Mechanics of Materials 153 (2021) 103672

Contents lists available at ScienceDirect

Mechanics of Materials

journal homepage: www.elsevier.com/locate/mechmat

A compressible plasticity model for pulp fibers under transverse load

Tristan Seidlhofer [a,d], Caterina Czibula [b,d], Christian Teichert [b,d], Ulrich Hirn [a,d], Manfred H. Ulz [c,d,*]

[a] Institute of Bioproducts and Paper Technology, Inffeldgasse 23, 8010, Graz, Austria
[b] Institute of Physics, Montanuniversitaet Leoben, Franz Josef-Str. 18, 8700, Leoben, Austria
[c] Institute of Strength of Materials, Kopernikusgasse 24/I, 8010, Graz, Austria
[d] Christian Doppler Laboratory for Fiber Swelling and Paper Performance, Graz University of Technology, 8010, Graz, Austria

ARTICLE INFO

Keywords:
Pulp fibers
Micromechanics
Poisson's ratio
Nanoindentation
Atomic force microscopy
Compression

ABSTRACT

In the progress of understanding the mechanical behavior of pulp fibers, advanced material models have to be developed alongside experimental investigations. The transverse behavior of pulp fibers is tested by atomic force microscopy (AFM)-based nanoindentation experiments to record both, the volume reduction and the force-displacement curve. Our measurements clearly indicate a compressible plastic behavior in conjunction with a highly nonlinear elastic behavior, both which are attributed to the nanoporous structure of pulp fibers. We therefore advocate a numerical model based on a compressible plastic model combined with a hyper-foam model. Our evaluation yields three key findings for the transverse behavior of pulp fibers: first, the compression behavior is dominated by plastic deformation and nonlinear elasticity, in agreement with the experimental indentation results; second, we found evidence that a compressible plasticity model is justified, with an estimated Poisson's ratio of 0.23; and third, a good agreement of our numerical model with out-of-plane compaction experiments from the literature for a sheet of paper was achieved.

1. Introduction

The investigation of mechanical properties of pulp fibers and paper sheets is an ongoing field of research. Mechanical models of paper- and other nonwoven materials are widely used in the development of converting processes (e.g. printing, creasing) and end use products (e.g. liquid containers, paper trays). Even though, the mechanics of paper is of primary importance, a deeper insight into the mechanics of its components – the single pulp fibers – is necessary for a better macroscopic understanding.

Thin paper sheets used in printing applications are bent or elongated and so are the fibers in the paper network. Consequently, in such applications the longitudinal tension mode of the fiber has been given a higher priority. For thick paper, paper board and carton which are used mostly in packaging applications, compression behavior is very relevant. Since the fibers are mainly oriented in the paper plane, the transverse compression behavior is dominating in high local deformations such as creasing, folding (Beex and Peerlings, 2009), converting processes, deep drawing (Wallmeier et al., 2015), and embossing. Therefore, an investigation into the compressible behavior of the fiber is of interest. This was primarily approached in the literature by investigating the geometrical deformation (e.g. lumen collapse) of the whole fiber. For instance, the fiber's transverse compression was studied with a simulation approach (Shiari and Wild, 2004; De Magistris and Salmén, 2008) and also in the context of fiber-to-fiber bond formation (Brandberg and Kulachenko, 2017). Consequently, further investigations into the compressibility modeling of the fiber material is of major interest.

Experimentally, the fibers' compressible behavior was investigated by several authors (Dunford and Wild, 2002; Hartler and Nyrén, 1970; Hardacker, 1969; Wild et al., 2005). These experiments revealed that the fiber is collapsing during compression. However, it is difficult to extract material parameters for the fiber wall, since only little is known about the geometry of the fibers in these experiments. The compressibility could be probed with a hydrostatic compression test for isotropic materials or a plane strain compression test for transverse isotropic materials (Christensen, 1980, Eq. 1.4). To the authors' best knowledge no hydrostatic compression tests for pulp fibers are available in the literature, which might be related to the difficulty of fiber preparation and the friction influence of the fixture. In contrast to fibers in wood blocks, it is difficult to alter the geometry of single pulp fibers and perform tests on a

* Corresponding author. Institute of Strength of Materials, Kopernikusgasse 24/I, 8010, Graz, Austria.
E-mail address: manfred.ulz@tugraz.at (M.H. Ulz).

https://doi.org/10.1016/j.mechmat.2020.103672
Received 23 April 2020; Received in revised form 20 October 2020; Accepted 21 November 2020
Available online 3 December 2020

well-defined geometry (Adusumalli et al., 2010b). Furthermore, classic experimental setups lack the ability to access the transverse direction of the fiber. Here, advanced techniques are necessary. With the development of depth-sensing techniques, the properties of the fiber surface became more accessible. First, conventional nanoindentation (NI) investigations were obtained on cross-sections of wood fibers (Wimmer et al., 1997; Gindl et al., 2004; Gindl and Schöberl, 2004; Adusumalli et al., 2010a; Eder et al., 2013; Jäger et al., 2011). In the last few years, atomic force microscopy (AFM) evolved into a useful technique for the characterization of pulp fibers (Fahlén and Salmén, 2005; Schmied et al., 2012; Nilsson et al., 2001; Yan and Li, 2013). The development of an AFM-based nanoindentation (AFM-NI) method enabled local access of the rough surface topography of single pulp fibers on the nanometer scale. Here, the influence of relative humidity and water on the elastic as well as plastic properties was studied for pulp fibers (Ganser et al., 2014; Persson et al., 2013; Ganser and Teichert, 2017). Additionally, an AFM-NI approach was developed to investigate the viscoelastic behavior of pulp fibers in transverse direction (Czibula et al., 2019; Seidlhofer et al., 2019).

1.1. Pulp fiber structure, nanoporosity, and surface morphology

A pulp fiber mainly consists of cellulose, lignin and hemicellulose. Small crystalline cellulose regions (nanocrystals) are forming a band by connecting with semi-crystalline regions (Bergander and Salmén, 2002; Salmén, 2018; Gibson, 2012). Several of these bands are in close proximity to each other and form a bundle – a so-called microfibril – which has a diameter of approximately 30 nm. These microfibrils further form larger fibril bundles which are mainly oriented along the fiber axis. As a result, the fiber has a significant strength difference in longitudinal and transverse direction.

In between the microfibrils a matrix consisting of lignin and hemicellulose is present. Both lignin and hemicellulose are rather soft compared to crystalline cellulose. Lignin is – in contrast to hemicellulose – a highly cross-linked hydrophobic polymer. It provides structural stability and limits the swelling of the matrix (Conners, 2001; Cristian Neagu et al., 2006; Booker and Sell, 1998).

Several cell wall layers are building up the fiber. These layers can be most prominently distinguished by the regularity of the orientation of the microfibrils. In contrast to the outer primary (P) wall, the secondary (S_1, S_2, S_3) walls have a regular microfibril structure. During chemical pulping, the thin P and parts of the S_1 wall are removed due to the high lignin content (Alava and Niskanen, 2006). Furthermore, the S_2 wall is the thickest layer of the total cell wall with the highest degree of microfibril alignment and represents about 80% of the cell wall (Salmén, 2018; Gibson, 2012).

Apart from lignin and hemicellulose the matrix of pulp fibers also consists of pores. Porosity of the matrix is strongly influenced by the pulping process. During kraft pulping, lignin is to a high percentage removed from the fiber wall, which results in a considerable increase of the pore volume (Stone and Scallan, 1965). Interestingly, even though for thermomechanical pulp in principal no lignin is removed, the pore volume still increases due to micro-cracks and delamination (Maloney and Paulapuro, 1999). The measurement of the pore size distribution in single pulp fibers is a tricky task and results obtained by several techniques can be found in the literature. Thermoporosimetry or adsorption of gases and polymers (Alince, 1990, 2002; Maloney and Paulapuro, 1999) have been frequently applied to pulp fibers. The reported values show a large pore diameter range, which depends on the moisture content and is influenced by sample preparation as well as the measurement technique. However, during drying capillary forces cause the collapse of macro pores and only small pores in the mesopore range ($<$ 50 nm (Lovikka et al., 2016)) remain (Park et al., 2006) at moderated moisture content.

The structural combination of nanopores, lignin and hemicellulose has a major influence on the transverse compression behavior of the fiber. The nanopores can collapse and the crystalline cellulose blocks can stack during mechanical compression. As a result, increasing stiffness with compression is to be expected. As an additional result, a compressible behavior is to be expected not only in the elastic but also in the plastic regime.

1.2. Scientific approach

Material development frequently makes use of incompressibility constraints to reduce the complexity of the model. Subjecting incompressibility is either physically motivated due to high compression to shear modulus ratios or due to a low impact of compressibility on the targeted application of the model (Seidlhofer et al., 2019). In compaction applications, incompressibility cannot be motivated for pulp fibers due to the present porosity. As a consequence, this has as well implications on the selection of an appropriate plasticity model: It has to be identified if the plastic deformation is volume preserving. Therefore, this work focuses on the quantification of the compressibility in transverse direction of the fiber in both the elastic and the plastic material behavior.

The compressibility of a solid body – a measure of its relative volume change as a response to a pressure – will play a major part in the following. If a material is compressible, the volume (or in a plane the area) will change. If a material is incompressible, the material will only be pushed aside to establish a volume preserving state. Consequently, the area change in a plane strain setting is a measure of the compressibility of the material (Fig. 1).

Here, we pursue a plane strain testing procedure in which both two-dimensional (2D) geometrical and one-dimensional (1D) force-displacement signals can be extracted. This way, sufficient information is provided to estimate compressibility parameters as, for instance, the Poisson's ratio.

Furthermore, we demonstrate the importance of the fibers' nanoporosity. As it is in most cases impractical to model nanopores geometrically in fiber simulations, the constitutive equations have to be enhanced. Therefore, we propose a nonlinear elastic model and a compressible plastic model to close this gap.

The structure of the article is as following. An introduction to relevant aspects of pulp fibers is given first. As this study combines numerical and experimental work, the subsequent methods section is divided into an experimental and a numerical modeling part. The link between experiments and model is established with suitable numerical optimization techniques. In the results section, an interpretation of the estimated parameters is given. Finally, a discussion closes this paper.

2. Methods

AFM-NI has advantages in contrast to classical NI: It enables the possibilities to measure the surface topography, to choose specific spots on the scanned surface for indentation experiments, and to re-scan the same position after the experiments again. This high local resolution can be used to determine the lateral displacement after indentation on rough surfaces.

In Fig. 2, several $5 \times 5\ \mu m^2$ AFM topography images are stitched together to present the characteristic surface morphology of a single, unbleached, spruce kraft pulp fiber. Since during the pulping process the

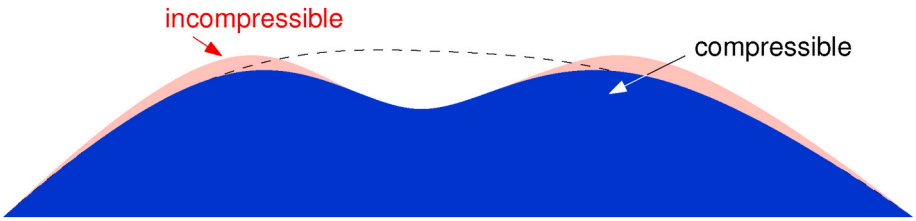

Fig. 1. The difference between an incompressible material and a compressible material during indentation is illustrated: If the material is incompressible, material is pushed aside to fulfill the volume preserving constraint.

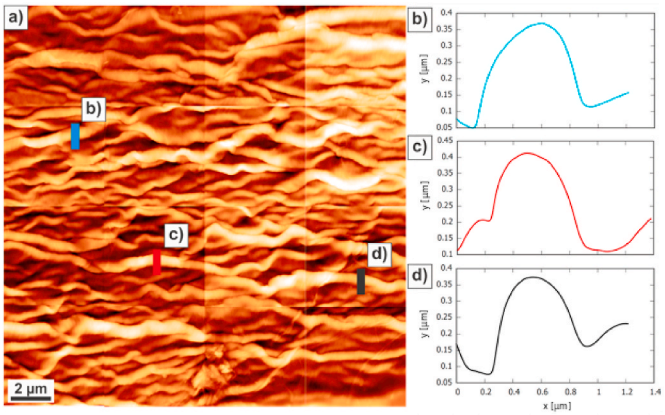

Fig. 2. Overview of the topography of an unbleached spruce kraft pulp fiber surface. (a) Three locations of wrinkles are indicated. Subfigures (b) to (d) give the corresponding wrinkle profiles that are averaged over 20 scan lines.

P and only few parts of the S_1 wall are removed, AFM measurements are usually performed on the S_1 wall (Ganser et al., 2014). As can be seen in Fig. 2, the fiber's surface is not smooth, but exhibits specific surface features – labeled wrinkles – which are caused by the drying-induced shrinkage of the fiber (Maloney and Paulapuro, 1999). During the drying process the fiber shrinks, which leads to surface instabilities, and wrinkles are preferably formed transversely to the stiff microfibrils. Consequently, it can be assumed that microfibrils are oriented perpendicular to the cross sectional plane of a wrinkle. In Fig. 2b–d, cross-sections of line scans of individual wrinkles are presented. These wrinkles have an average width of about 500 nm and are about 200 nm in height. Their length can be several µm. In Appendix A a further discussion on the microfibril alignment is given.

If an indentation is performed on the wrinkle, then – due to the stiff out-of-plane material behavior and the assumption of having long wrinkles – deformation is preferred in the cross section. Hence, a plane strain state can be assumed. A further discussion on the plane strain assumption is given in Appendix C. The AFM probe and a wrinkle of a fiber surface are illustrated in Fig. 3. This indentation experiments require due to the complex boundary conditions appropriate models to investigate material parameters. Whereas for flat surfaces 1D analytical based models tend to be sufficient (Fischer-Cripps, 2000; Ganser and Teichert, 2017; Chang and Liu, 2018), for arbitrarily curved surfaces in general a 2D simulation is required. Hence, the following methods section is divided into an experimental and a simulation part.

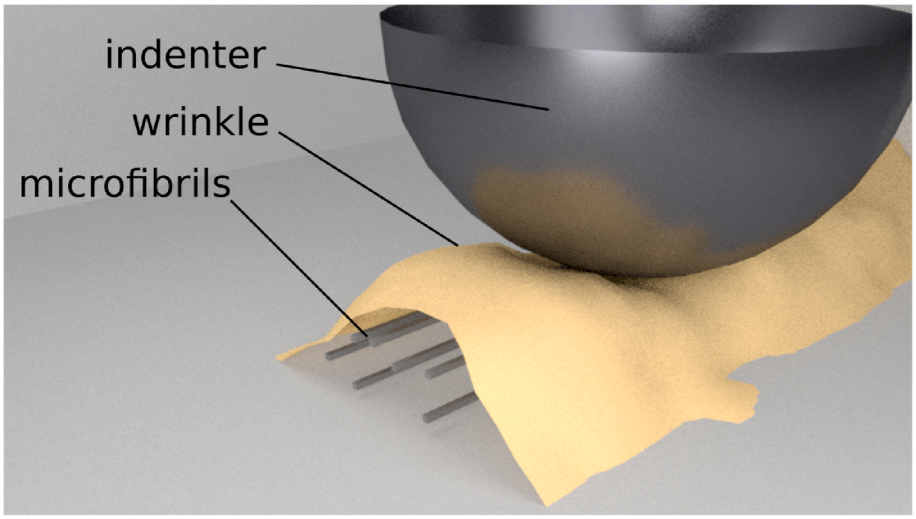

Fig. 3. Schematic visualization of an indentation of a wrinkle on the fiber surface. The indentation process can be idealized as a plane strain problem.

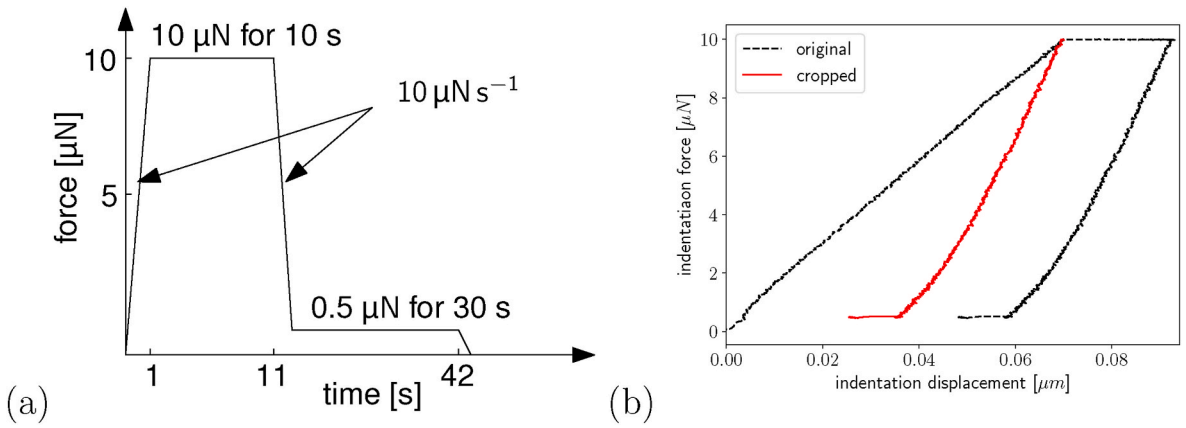

Fig. 4. (a) Load schedule of the AFM-NI experiment. (b) The experimentally obtained force-displacement curve was cropped to remove rate effects in the modeling. Exemplarily a typical curve is shown.

2.1. Experimental setup

All AFM-NI and AFM topography measurements have been obtained with an Asylum Research MFP-3D AFM equipped with a closed-loop planar x-y-scanner. For AFM-NI, ND-DYIRS full diamond probe (Advanced Diamond Technologies) were used. The tip geometry of the probe is evaluated by scanning an NT-MDT TGT01 calibration grid (an array of sharp spikes) and utilizing the tip-sample dilation principle (Villarrubia, 1994; Ganser and Teichert, 2017). These probes feature a regular, four-sided pyramid as a tip. The angles between the pyramidal faces are about 75°, and the apex radius is about 50 nm. This scanned tip geometry was used for the indenter geometry in the simulation. The spring constant of the cantilever was determined with the thermal sweep method (Hutter and Bechhoefer, 1993) to be 87.38 Nm^{-1} with a resonance frequency of 386.6 kHz and a Q-factor of 572. All measurements were carried out at a controlled relative humidity (RH) of 50 % in a closed AFM fluid cell and at a temperature of 23 °C. Data analysis of the topography had been obtained with the open-source software Gwyddion (Nečas and Klapetek, 2012).

The load schedule (Fig. 4a) consisted of fast loading and unloading

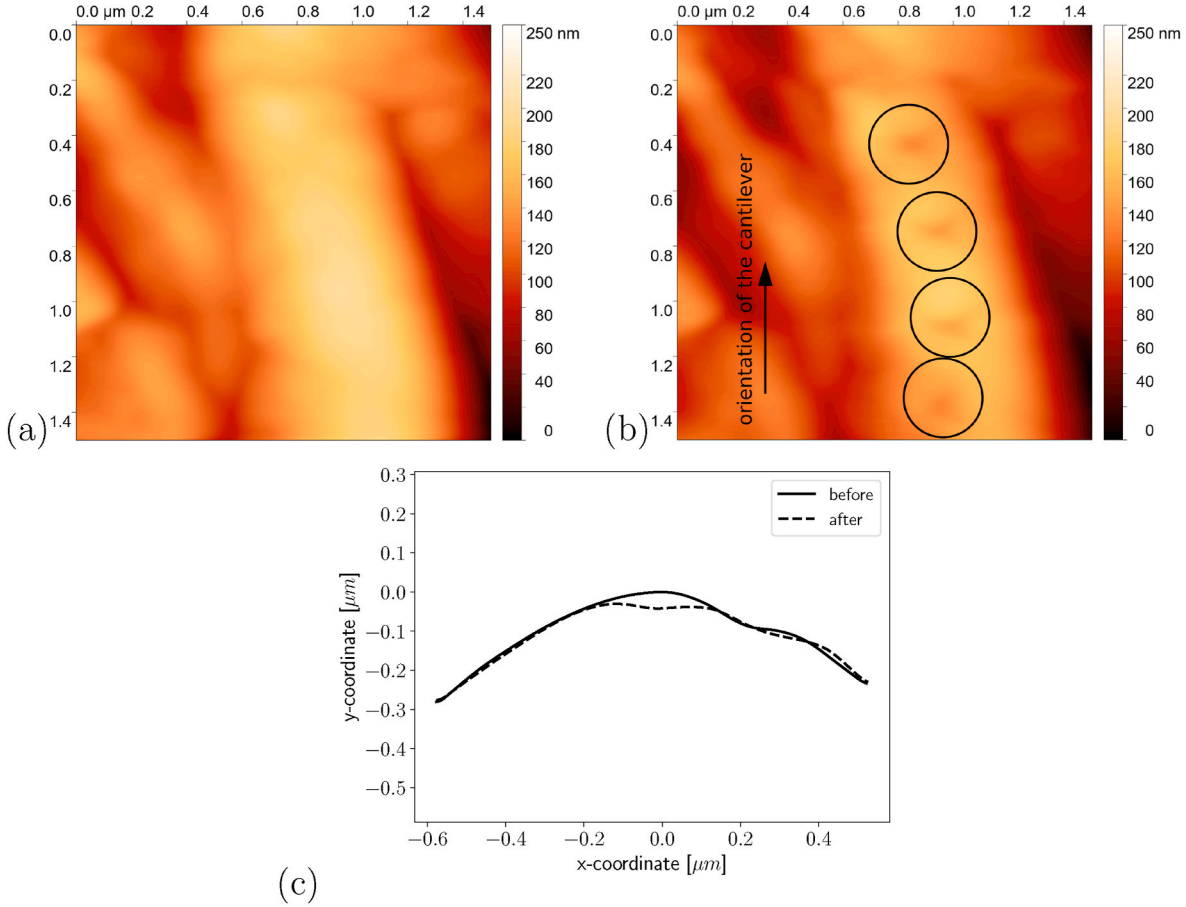

Fig. 5. Surface topology of a fiber wrinkle before (a) and after (b) the nanoindentation. Typical curves of the measured contours (c) indicate a decrease of volume by the permanent deformation.

ramps and two different holding periods. The loading and unloading rate was 10 μNs^{-1}. At maximum load, a holding period of 10 s was necessary allowing dynamic effects to decay in order to obtain an undistorted unloading ramp (Feng and Ngan, 2002; Tang and Ngan, 2003; Gindl et al., 2004). Since pulp fibers are viscoelastic, the material softened during the holding period and thus the indentation depth increased. This additional deformation was recovered completely after removing the load in most cases. We simplified the evaluation by cropping out the holding part in the signal to prevent the inclusion of rate effects in the modeling, which is sketched in Fig. 4b. Therefore, we postulate that the shifted unloading part represents the instantaneous unloading without viscoelastic material history.

A representative surface topography of the wrinkle before and after the AFM-NI experiment is presented in Fig. 5a and b. Permanent indents reflecting the four-sided pyramidal shape of the AFM tip are clearly visible. Furthermore, the measured wrinkle's geometry before and after the nanoindentation shows a significant decrease in volume.

2.2. Material model

The complexity of the material model is motivated by experimental observations (compare Fig. 4b). First, the force-displacement curves show in the unloading branch a considerable curvature, which cannot be explained by the contact nonlinearity. As this branch is solely determined by the elastic part of the model, nonlinear elasticity has to be introduced. Second, plastic deformation is observed and a residual volumetric change (compare Fig. 5c). This motivates the introduction of a volumetric plastic contribution.

To simulate the observed experimental behavior, a model has to be established which is suitable to handle finite strains and which includes two parts. The first part models a nonlinear elastic constitutive behavior and the second part includes a Green-type plasticity yield criterion (also known as crushable plasticity).

The nonlinear elastic behavior is mainly implied by the microstructure. Homogenization strategies as for instance (Morin et al., 2018; Godinho et al., 2019), which were successfully applied to fibrous materials, are an interesting alternative to phenomenological models. However, we adopt a phenomenological description in this work, which is with respect to parameters fitting presumably more appropriate. For the description of thermodynamically based nonlinear elastic behavior at finite strains, either hyperelasticity – which is in stress rate-form a special case of hypoelasticity according to the definition (Truesdell et al., 2004, Eq. 99.1 & 99.2) – or a rather recent approach on implicit rate-type models (Rajagopal and Srinivasa, 2009, 2011; Rajagopal, 2007) can be motivated. Implicit non-dissipative rate-type models are under special circumstances advantageous as for instance for incompressibility or instant stiffness increase (Rajagopal, 2007). In this work, material isotropy is assumed due to the transverse testing, the reduced compound effect implied by pores and the plane strain assumption (see also Appendix C). Furthermore, we hypothesize the existence of a free Helmholtz energy (elastic potential) that can describe the experimental response very well. The hyper-foam elastic potential fulfills these requirements. For the treatment of plastic behavior we propose the existence of a yield surface. Hence, the model falls in the constitutive class of hyperelasto-plasticity, a class which is next to hypoplasticity and endochronic plasticity (Kolymbas, 1991; Kolymbas and Medicus, 2016; Suchocki and Skoczylas, 2016). The latter two are better suited for problems with complex load path dependence or poorly defined elastic limit, as it is encountered for instance in soil mechanics (Medicus and Schneider-Muntau, 2019; Medicus et al., 2019) or hysteresis effects in rubber (Netzker et al., 2010).

Finite deformation theory requires the definition of a nonlinear map $\phi : (\boldsymbol{X}, t) \mapsto \phi(\boldsymbol{X}, t)$ which maps a point $\boldsymbol{X}$ of the reference configuration $\mathscr{B}_0$ onto a point $\boldsymbol{x}$ of the spatial configuration $\mathscr{B}_t$ at time t. The deformation of infinitesimal elements is governed by the deformation gradient $\boldsymbol{F} := \frac{\partial \boldsymbol{x}}{\partial \boldsymbol{X}}$. The volume change is characterized by the Jacobian $J := \det(\boldsymbol{F})$, which must be strictly positive $J > 0$. An appropriate dimensionless description of deformation requires the definition of suitable strain measures. In this study, Hencky strains of the Seth-Hill family are applied which enables an additive finite strain elasto-plastic approach (Miehe et al., 2002). The relation between the Lagrangian Hencky strain tensor and the logarithmic stretches is given as:

$$\boldsymbol{E}_{\ln} = \sum_{i}^{N} \Lambda_i \boldsymbol{N}_i \otimes \boldsymbol{N}_i. \tag{1}$$

The quantity $\boldsymbol{N}_i$ is the i-th eigenvector of $\boldsymbol{E}_{\ln}$, and the logarithmic principal stretches Λ_i give the eigenvalues of the Hencky strain tensor. The total logarithmic strain is decomposed into an elastic and a plastic part

$$\boldsymbol{E}_{\ln} = \boldsymbol{E}^{\mathrm{e}}_{\ln} + \boldsymbol{E}^{\mathrm{p}}_{\ln}. \tag{2}$$

The elastic potential of the hyper-foam material (Dhondt, 2004) includes the principal stretches λ_i. These are substituted by its logarithmic counterpart $\Lambda_i = \ln(\lambda_i)$. Similar the Jacobian J can be expressed by the principal logarithmic stretches $J = \exp(\Lambda_1 + \Lambda_2 + \Lambda_3)$. As a result, we write the elastic potential of the hyper-foam material as

$$\psi = \frac{2\mu}{\alpha^2}\left(e^{\Lambda^{\mathrm{e}}_1 \alpha} + e^{\Lambda^{\mathrm{e}}_2 \alpha} + e^{\Lambda^{\mathrm{e}}_3 \alpha} - 3 + \frac{1}{\beta}\left(J_{\mathrm{e}}^{-\alpha\beta} - 1\right)\right); \tag{3}$$

where the arameter α governs the degree of nonlinearity, μ is the shear modulus, Λ^{e}_i the elastic principal logarithmic stretch of $\boldsymbol{E}^{\mathrm{e}}_{\ln}$ and $J_{\mathrm{e}} = \exp\left(\mathrm{tr}\left(\boldsymbol{E}^{\mathrm{e}}_{\ln}\right)\right)$ the elastic Jacobian. The parameter β can be evaluated with the elastic Poisson's ratio ν (Storåkers, 1986, Eq. (8)) as $\beta = \nu/(1 - 2\nu)$.

The first derivative of the elastic potential (Eq. (3)) with respect to the logarithmic strains yields the logarithmic stress tensor $\boldsymbol{S}_{\ln}$:

$$\boldsymbol{S}_{\ln} = \frac{\partial \psi}{\partial \boldsymbol{E}^{\mathrm{e}}_{\ln}}. \tag{4}$$

This stress tensor will be converted to the Cauchy stresses for output purposes in a later stage of the material routine (Miehe et al., 2002).

An elliptic yield criterion was used in early studies (Green, 1972) modeling a volumetric contribution to plastic deformation for porous solids. Recently this was employed by (Fritzen et al., 2013) and, in a modified form, also within the context of Hencky strains (Zerbe et al., 2017). Extensions to isotropic hardening were developed by (Deshpande and Fleck, 2000) and are available in commercial codes (Simulia, 2009). We give the Green type plasticity yield criterion as

$$f = \sqrt{q^2 + R^2 p^2} - y(\alpha_{\mathrm{h}})\sqrt{1 + \left(\frac{R}{3}\right)^2}; \tag{5}$$

where q represents the deviatoric equivalent stress (von Mises stress) and p the hydro-static stress:

$$q = \sqrt{\frac{3}{2}\boldsymbol{S}'_{\ln} : \boldsymbol{S}'_{\ln}},\ p = -\frac{1}{3}\mathrm{tr}(\boldsymbol{S}_{\ln}),\ \boldsymbol{S}'_{\ln} = \boldsymbol{S}_{\ln} + p\boldsymbol{1}. \tag{6}$$

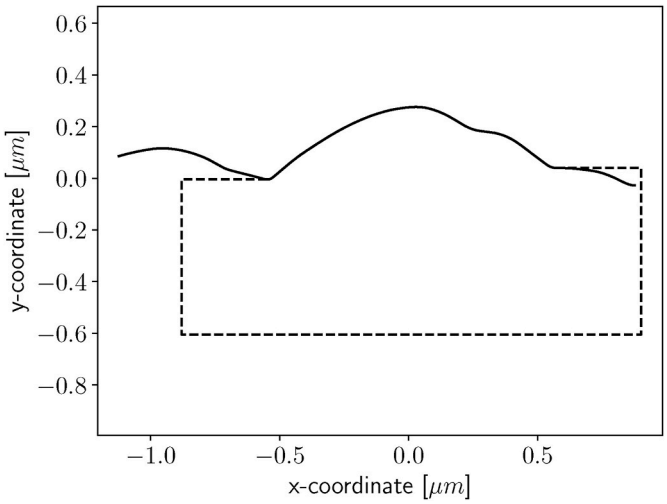

Fig. 6. Definition of the wrinkle geometry for the simulation input. The solid line represents the experimental data, the dashed line the geometry in the numerical model.

The yield surface ellipticity R is related to the plastic Poisson's ratio ν_p (Deshpande and Fleck, 2000, Eq. (5)):

$$R = \frac{3}{\sqrt{2}}\sqrt{\frac{1-2\nu_p}{1+\nu_p}}. \tag{7}$$

Furthermore, a linear hardening model is proposed:

$$y(\alpha_h) = y_0 + K\alpha_h; \tag{8}$$

where y_0 is the initial yield stress, K the hardening slope, and α_h the internal hardening variable.

The yield function is defined with the logarithmic stress tensor, and consequently the estimated yield strength y_0 and hardening parameter K are measured in logarithmic stresses. However, benchmarks show that the deviation from a multiplicative plasticity approach are small (Miehe et al., 2002). As a consequence, a comparison to other models using, e.g., the Mandel stress, is within bounds possible. In the special case of small strains, the difference between the stress measures vanishes.

Following standard arguments, the evolution of plastic strains $\boldsymbol{E}_p$ is proposed to follow an associative flow rule. With the plastic multiplier $\dot{\gamma}$, the evolution of the plastic variables can be given as:

$$\dot{\boldsymbol{E}}^p_{ln} = \dot{\gamma}\frac{\partial f}{\partial \boldsymbol{S}_{ln}}, \quad \dot{\alpha}_h = \dot{\gamma}. \tag{9}$$

2.3. Simulation

The AFM-NI experiment on surface wrinkles of pulp fibers was modeled by the finite element method (FEM). The topology of the wrinkle needed to be spatially discretized. As mentioned earlier, the wrinkles are elongated bumps on the surface, and the indentation process can be approximated by a 2D plane strain problem. The hybrid mesh – consisting in most parts of linear quad elements and few linear triangle elements – was generated with a characteristic element edge length of 8 nm. With respect to the force-displacement needed and the topography information, this coarseness was sufficient. To keep the influence of the boundary fixation minor, the topography was on the right and left sides extended with 30% of the wrinkle width and the bottom was extended by a fixed value of 0.6 µm, which is approximately twice the wrinkle height. Fig. 6 shows the creation of such an area to be meshed with Gmsh (Geuzaine and Remacle, 2009).

The simulations were carried out with code_aster 14.4 (EDF, 2020) and the material routine interface Mfront (Helfer et al., 2015). For the surface interaction between the indenter and the fiber surface, a friction coefficient of 0.26 was assumed according to (Bogdanovic et al., 2001). Due to the high incompatibility of the surface curvatures a penalty-based contact algorithm was selected. The boundary conditions for the simulation are displayed in Fig. 7. The indenter was modeled as an undeformable body and its axis was fixed in horizontal direction. Since the movement of the AFM cantilever in vertical direction was very small compared to the cantilever's length, this simplification – of neglecting a slight rotation of the indenter – is valid. The indentation force was vertically applied to the indenter. Since in a plane strain problem the subjected force is applied per unit length, the force has to be divided by the thickness. The effective thickness is computed from the maximum

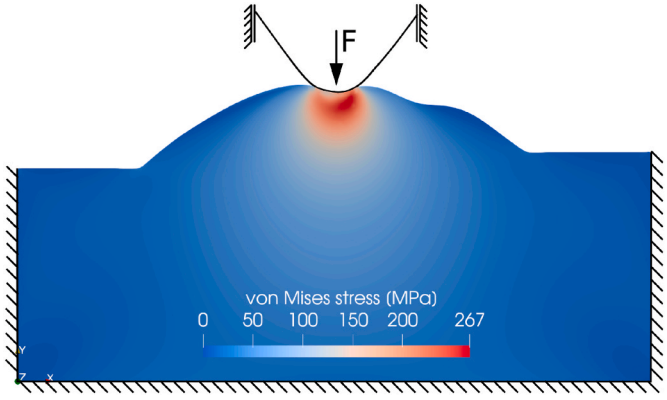

Fig. 7. Boundary conditions and simulation of the nanoindentation experiment.

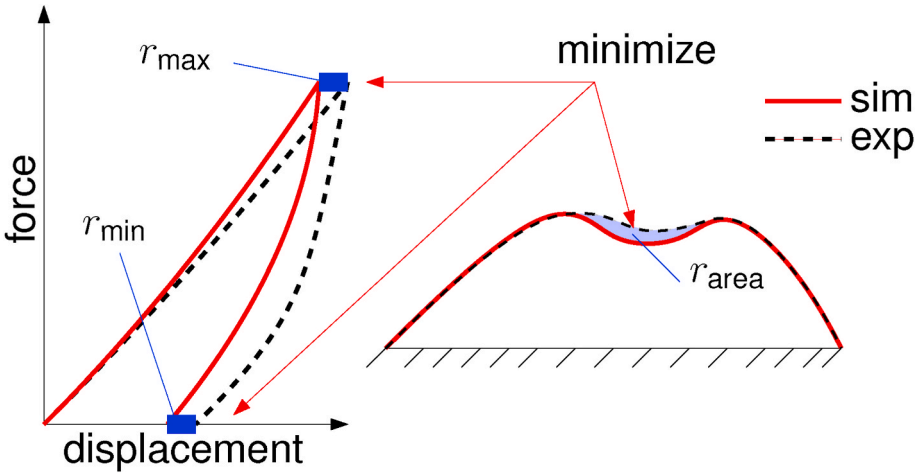

Fig. 8. Definition of three differences to fit the simulation and experiment.

indentation depth of the respective experiment and the indenter geometry. See Appendices B and C for a detailed explanation and a comparison with a three-dimensional simulation.

2.4. Optimization

The material model in Section 2.2 comprises six parameters (μ, α, ν, ν_p, y_0, K). For the optimization, the parameter set was reduced to three (μ, ν, K) by setting the exponent α for the elastic nonlinearity and the yield strength y_0 to a fixed value as well as the elastic and plastic Poisson's ratios ν and ν_p to be equal. The fixed value for α was determined by choosing a value that shows in the relevant strain domain (approximately up to 30 %) a visible nonlinear effect, which was $\alpha = 60$ in this study. Therefore, this exponent turned out to have a larger value for pulp fibers as it would normally be the case for very soft and extensible foams ($\alpha = 3 \ldots 7$ (Kim et al., 2019)). Besides, a constant exponent ensured also a better comparability between the fitted Young's moduli. The fixed value for the yield strength y_0 was motivated by the fact that no clear yield point can be detected for pulp fibers (Dumbleton, 1972; Sedighi-Gilani and Navi, 2007) and that y_0 and K had to be interpreted in combination. A remedy for this problem was to set a suitable value for y_0 for all experiments, which turned out to be $y_0 = 50$ MPa. The connection between K and y_0 will be further discussed in Section 3. By equating ν with ν_p it is assumed that the difference in

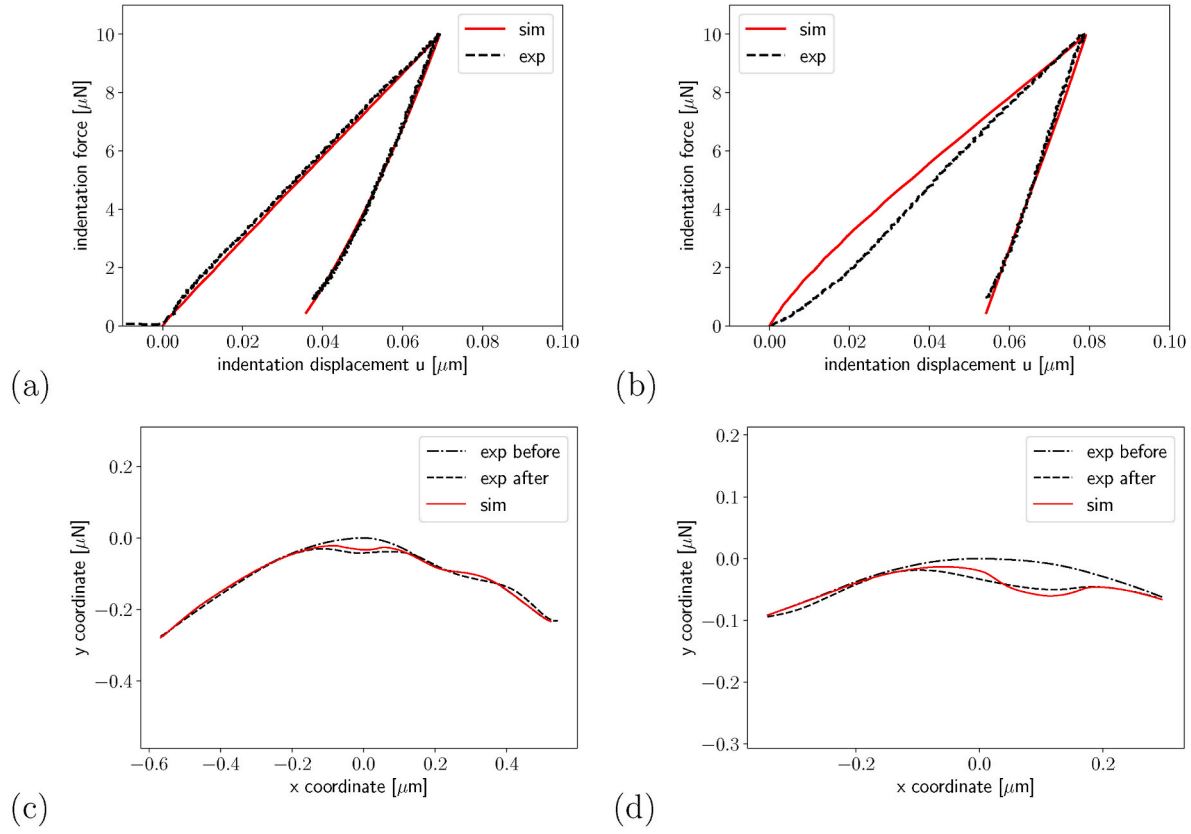

Fig. 9. Difference of the two quality groups. (a,b) Typical fits of the force-displacement curves. (c,d) Comparison of the simulated topology and the measured topology. (a,c) Quality group I and (b,d) quality group II.

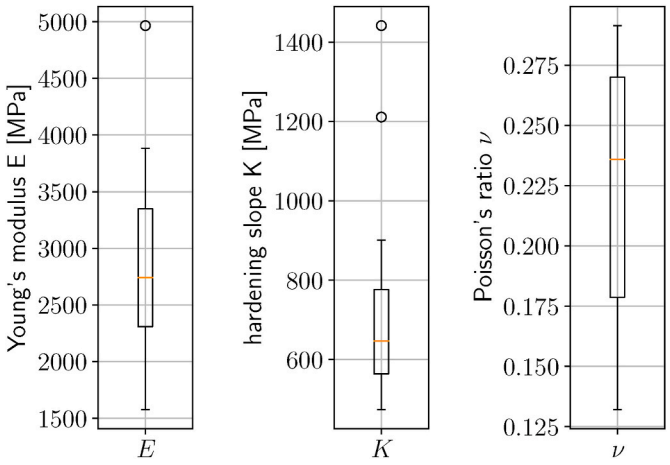

Fig. 10. Box plot of the optimization parameters E, K and ν.

lateral contraction during plastic and elastic deformation is negligible at small strains. This can be especially motivated in the beginning of the compaction phase since part of the pore volume reduction is irreversible which does not alter the apparent lateral contraction. At larger strains, the Poisson's ratio is known to be strain dependent for porous and foam materials (Sanborn and Song, 2019; Patterson et al., 2015; Rinde, 1970). This nonlinearity is accounted for in the hyper-foam strain energy function in Eq. (3). Therefore, the apparent elastic Poisson's ratio will be naturally different at higher strains to the plastic Poisson's ratio ν_p.

For the optimization, an appropriate objective function $F(\mu, K, \nu)$ had to be presented. Three differences between estimated and true values were defined for this purpose. Fig. 8 presents two displacement type differences between the error at maximum force (r_{max}) and at a hold load of 0.9 µN (r_{min}), respectively. Additionally, the difference between the deformed cross sectional areas A_{exp} in the experiment and A_{sim} in the simulation was defined. The area itself was computed with the Gauss's area formula. To maintain consistent units, the displacement errors were normalized by the constant experimental displacement $d_{0.9\mu N}$ at 0.9 µN and the area error with the experimental undeformed cross sectional area $A_{undeform}$.

$$r_{area,n} = \frac{A_{exp} - A_{sim}}{A_{undeform}}, \quad r_{max,n} = \frac{r_{max}}{d_{0.9\mu N}}, \quad r_{min,n} = \frac{r_{min}}{d_{0.9\mu N}}. \tag{10}$$

The objective function is the sum of squares of all three differences previously defined multiplied with a factor of 100 to ensure good scaling:

$$F = \left(100\, r_{area,n}\right)^2 + \left(100\, r_{min,n}\right)^2 + \left(100\, r_{max,n}\right)^2. \tag{11}$$

The optimization problem was solved within the OpenMDAO framework 3.0.0 (Gray et al., 2019) which provides a comprehensive interface to several optimization strategies. For this study, a sequential least squares programming (SLSQP) algorithm of the SciPy package (Virtanen et al., 2020) was utilized. Since the parameters have different magnitudes and sensitivity an appropriate scaling procedure was applied (Gill et al., 1981) to optimize all parameters at once.

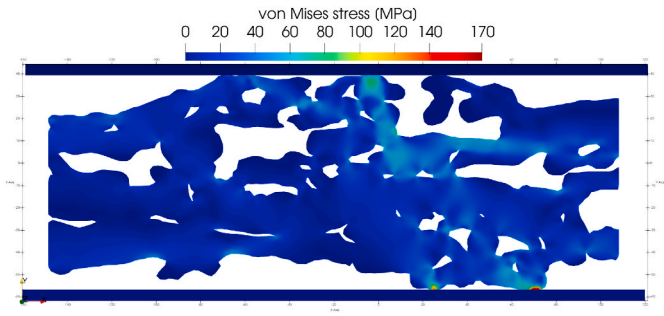

Fig. 12. Compaction of a sheet of paper. Paper cross section at mean compaction pressure of 3.528 MPa.

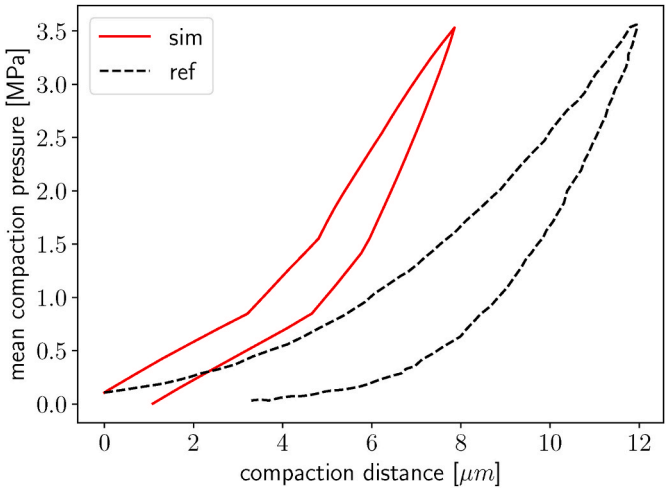

Fig. 13. Comparison of a typical force-displacement curve of Chen (2016) with the numerical simulation.

3. Results

In this study, 17 individual indents on 8 wrinkles were analyzed. Spruce fiber samples were extracted from unbleached unrefined kraft pulp from industrial production by Mondi Frantschach, Austria.

A comparison of the cross section before and after the indentation yields an area reduction of 17 % on average. However, it should be noted that this value is only indicating the order of magnitude of the compaction but is not fully representative as a total value, since the compaction with the indenter leads to a highly inhomogeneous compression field in the solid. Hence, the compaction could be locally considerably higher.

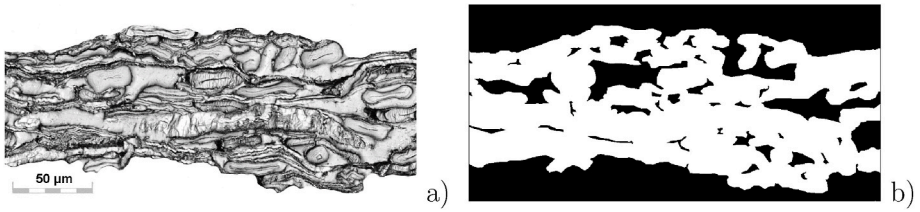

Fig. 11. Cross sectional geometry of a paper sheet. Manual pore volume detection by binarization (b) of a microscope image (a). Some fibers are cut longitudinally, and they move at some point out-of-plane. It is assumed that they are still close to the cutting plane, and therefore this region is not accounted for as pore volume.

3.1. Estimated material parameters by optimization procedure

The results of the fitting procedure were classified into two quality groups (compare Fig. 9). In group I, consisting of 10 indentation experiments, both force-displacement and topological deformation matched each other very closely. The remaining 7 indentations form group II, in which the fits did not overlap very well. An overview of the data is provided in the electronic supplementary information.

As mentioned above, the values $\alpha = 60$, $y_0 = 50$ MPa and $\nu_p = \nu$ were fixed. Since the shear modulus μ is not an appropriate parameter to be compared with values in the literature, the shear modulus was converted to the Young's modulus $E = 2\mu(1+\nu)$ (Dhondt, 2004). Therefore, the fitting procedure resulted in optimized values for the hardening slope K, the Young's modulus E, and the Poisson's ratio ν.

The obtained material parameters are presented in Fig. 10. The scattering of values for E and K are within a reasonable range as a strong natural variation of mechanical properties is to be expected (Mark, 1983; Niskanen, 1998). The distributions of E, K and ν are slightly skewed which can be attributed to the sample number. Most importantly, the Poisson's ratio is clearly indicating a compressible behavior.

The fitted parameters of the numerical model are interdependent. A discussion of this interdependency and its influence on the optimization strategy is given in Appendix D.

3.2. Numerical example

In this section a numerical example of an out-of-plane paper compaction is presented. We prove this way the suitability for complex applications of both the numerical model, i.e. a hyper-foam material model and Green-type plasticity model, and the precedingly fitted parameters, i.e. the fitting strategy to experimental data. A representative paper cross sectional structure was generated out of a microscope cross section image of a paper microtome cut (Fig. 11) (Lorbach et al., 2012). The detection of the pore volume was done manually. During that procedure, it was assured that all fibers are interconnected with each other. We compare the obtained numerical results qualitatively with the experimental work of Chen (2016, Fig. 2.5(a)) and Chen et al. (2018).

The paper segment had a width of 256.6 μm and a height of 104.4 μm. The horizontal movement of the sides was restricted. An equivalent compaction force was computed to achieve the same mean contact pressure of the flat punch of the reference data (Chen, 2016, Fig. 2.5(a)). The zero point was set to the preload of the reference data. Furthermore, the material parameters as found in the previous section were used in this simulation. A compacted state of the cross section is given in Fig. 12.

Fig. 13 presents a typical force-displacement curve of Chen (2016) and compares it with the corresponding curve obtained by the numerical simulation. Besides both curves show an alike shape, the simulation exhibits kinks due to the small sample and the lack of a statistically smooth pore structure and surface. The difference in the total compaction (compaction distance) can be attributed to various reasons: a different pore structure was present in the experiment; no filler material was considered; a smaller sample size was investigated in the simulation; the specific friction coefficient between punch and paper was not known and was set to the same value 0.26 as used in the preceding parameter evaluation. Considering both, that the parameters are extracted from single fibers and that the simulation results are in the same order of magnitude as macroscopic experiments (the resultant Young's modulus is too high by about a factor of two), this example motivates further investigation of single fiber properties and suitable material models.

Fig. 11b offers an interesting observation in combination with Fig. 13. The load is transferred locally through bands (force chains) from the top to the bottom. Consequently, the regions with low slope in the force-displacement curve are determined by the geometrical pore collapses, and regions with increased slope are derived by the compaction of the fiber material.

4. Conclusions

Wrinkles are formed on the pulp fiber surface during drying due to surface instability effects. These wrinkles were used in this work to extract both topological and force-displacement information out of AFM-NI experiments. On the simulation side, we utilized a Green type yield criterion in combination with a hyper-foam material. The material parameters were estimated by an optimization approach. The optimization of the full set of parameters was avoided by identifying the influence of the parameters on the force-displacement curve. As a result, two of the parameters could be set to predefined values and two additional parameters could be set equal by assuming that the plastic Poisson's ratio is equal to the elastic one. The remaining three parameters were well related to three appropriate error definitions in the objective function which ensured that the optimization converged to a unique solution.

Within the force schedule employed, the maximum force was held for 10 s. During this holding period creep was observed. To a certain extend this creep was reversible after unloading, thus it seemed reasonable to remove the hold period for further analysis. A consequence by this simplification is the underestimation of the contact area. The influence of the contact area is especially high at the beginning of contact, since there is a singularity present. With the progress of indentation depth, the material deformed plastically and consequently the contact area increased less as it would have been the case with a linear elastic material model and Hertz theory (proportional increase) (Johnson, 1985). Hence, the deviation is expected to be negligible.

Nonlinear elasticity was used in several studies concerning out-of-plane compaction of paper (Borgqvist et al., 2015; Li et al., 2018). In addition fiber network simulations indicate as well an exponential behavior (Hossain et al., 2019; Chen and Siegmund, 2019). Even though the fibers are on a different length scale, a similar mechanism seems to be present. Compared to previous works (Czibula et al., 2019; Seidlhofer et al., 2019) the Young's modulus is in the same range. However, it must be noted that the Young's modulus is estimated in classic depth sensing nanoindentation theory in the upper part of the unloading curve (Oliver, W.C. and Pharr, 1992). Since the material exhibits nonlinear elastic behavior, the tangent modulus is much higher at higher strains than in the initial state. Since in this study the initial modulus is used as a parameter, a direct comparison is not possible.

The limitations of this work are determined on one hand by the measurement accuracy and on the other hand by the numerical and modeling assumptions. Due to the finite size of the AFM cantilever tip, i.e. the indenter, the detection of the surface topology was subjected to dilation and the topography was blurred. In the force-displacement signal, viscoelastic effects were removed. This was justified by observations that the deformation recovered after unloading and the contact area error could be neglected due to plastic deformation. The measurements were performed on the surface of the fiber. The porosity in the center of the fiber could be different and consequently the compressibility lower.

The major finding of this study is that during compaction of pulp

fibers at very low loads already plastic deformation occurred. We attribute this effect to the presence of nanopores in the fiber wall. Additionally, we observed that a residual volume loss was present, which was an indication that some pores irreversibly collapsed. Similar to an out-of-plane paper compression test (Chen, 2016), a nonlinear elastic behavior was observed. The nonlinearity could be explained by formation of force chains of stacked microfibrils and the reversible collapse of nanopores. Force chains are commonly observed in granular materials (Peters et al. (2005); Kuhn (1999)). In this case, the microfibrils would take the role of the stiff particles in a soft matrix. The initial elastic nonlinearity on the paper level is dominated by the macropores. However, in a later stage of compaction the fibers' compressibility will gain in importance. Plastic deformation is for most mechanical finishing treatment of paper the relevant state to be achieved. As these treatments are locally concentrated, the fibers' plastic compressibility will lead in general to a softer behavior. Therefore, compressible plastic fiber models are expected to provide better results.

Author statement

Tristan Seidlhofer: Conceptualization, Methodology, Software, Validation, Visualization, Formal analysis, Writing – original draft, Writing – review & editing. Caterina Czibula: Conceptualization, Methodology, Investigation, Visualization, Data curation, Writing – original draft, Writing – review & editing. Christian Teichert: Resources, Writing – review & editing. Ulrich Hirn: Resources, Project administration, Funding acquisition, Writing – review & editing. Manfred H. Ulz: Conceptualization, Methodology, Supervision, Writing - original draft, Writing - review & editing.

Declaration of competing interest

The authors declare that they have no known competing financial interests or personal relationships that could have appeared to influence the work reported in this paper.

Acknowledgements

The financial support by the Austrian Federal Ministry for Digital and Economic Affairs and the National Foundation for Research Technology and Development is gratefully acknowledged. We also thank our industrial partners Mondi Group, Canon Production Printing, Kelheim Fibres GmbH, SIG Combibloc Group AG for fruitful discussions and for their financial support.

Appendix A Microfibril alignment and angle

It is assumed that wrinkles are preferably formed in such a way that the microfibrils are aligned along the wrinkle depth (i.e., the wrinkles on the fiber's surface are parallel to the microfibrils). A visualization with a connection of wrinkle orientation to the microfibril angle (MFA) is given in Fig. A14. Therefore, the microfibrils point in out-of-plane direction of a wrinkle's cross section. As a result, the testing procedure is perpendicular to the microfibril reinforcement and this suggests that mainly the transverse behavior of the fiber is tested. It is clear that any misalignment has an influence on the results. However, this misalignment's effect is considered to be negligible.

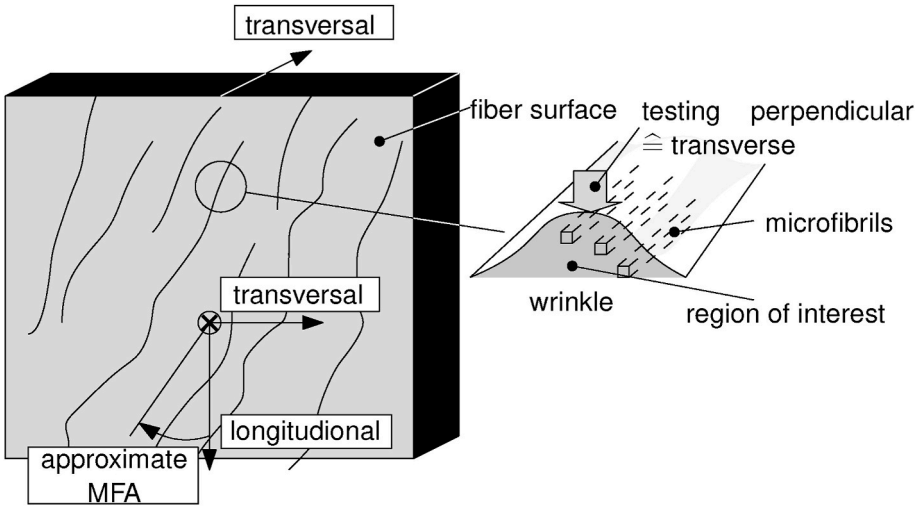

Fig. A.14. Orientation of the microfibrils alongside the wrinkle length.

Appendix B Effective thickness

The effective thickness for the plane strain simulation can be approximated by the projected out-of-plane contact arc length (Fig. B15 (a)). This length can be estimated by assuming a flat out-of-plane extension of the wrinkle's cross section and the given indenter's geometry. This assumption implies a fixed relation between the projected arc length and the indentation depth as shown in Fig. B15 (b). With this relation and taking the maximum indentation depth of the experiment into account, the projected arc length can be identified and used as the effective thickness.

AFM nanoindentation measurements on pulp fibers have shown that the adhesion forces have a magnitude of 0.1 μN to 0.9 μN (Czibula et al., 2019) and are, therefore, comparable to the applied 10 μN. Since in out-of-plane direction the wrinkle surface is less curved and consequently the

contact pairs are closer to each other, preferably an adhesion meniscus is formed (Kendall, 2001; Barthel, 2008) (see Fig. B15 (a)). This meniscus leads to a non-zero initial contact area. One experimental indication for this effect is the lack of a convex shape in the initial force-displacement curve. Therefore, the used constant thickness can be justified as an implicit consideration of adhesion effects.

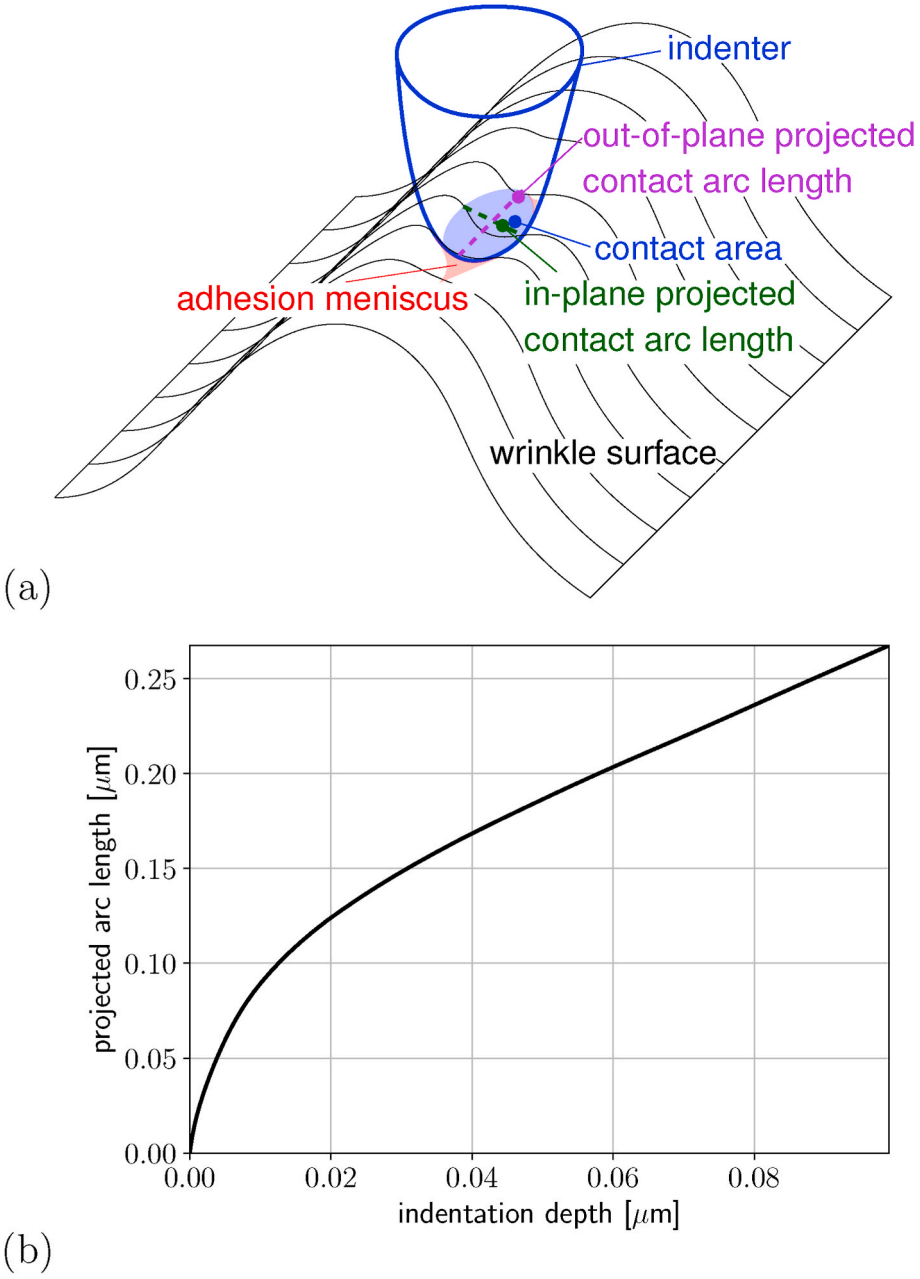

Fig. B.15. (a) Illustration of the projected contact area on a wrinkle. The out-of-plane contact arc length extends differently than the in-plane contact arc length. Adhesion forces implicate an increased contact area due to a forming meniscus. (b) Projected out-of-plane contact arc length with respect to the indentation depth.

Appendix C. Plane strain assumption

To validate the plane strain assumption, a three-dimensional simulation was carried out with the evaluated parameters from the plane strain fit of the data set presented in Fig. 9 (a) & (c). The required three-dimensional geometry was generated by an extrusion of the two-dimensional wrinkle topology in out-of-plane direction by 1/3 of the wrinkle width. The displacements of the bottom and side faces were fixed.

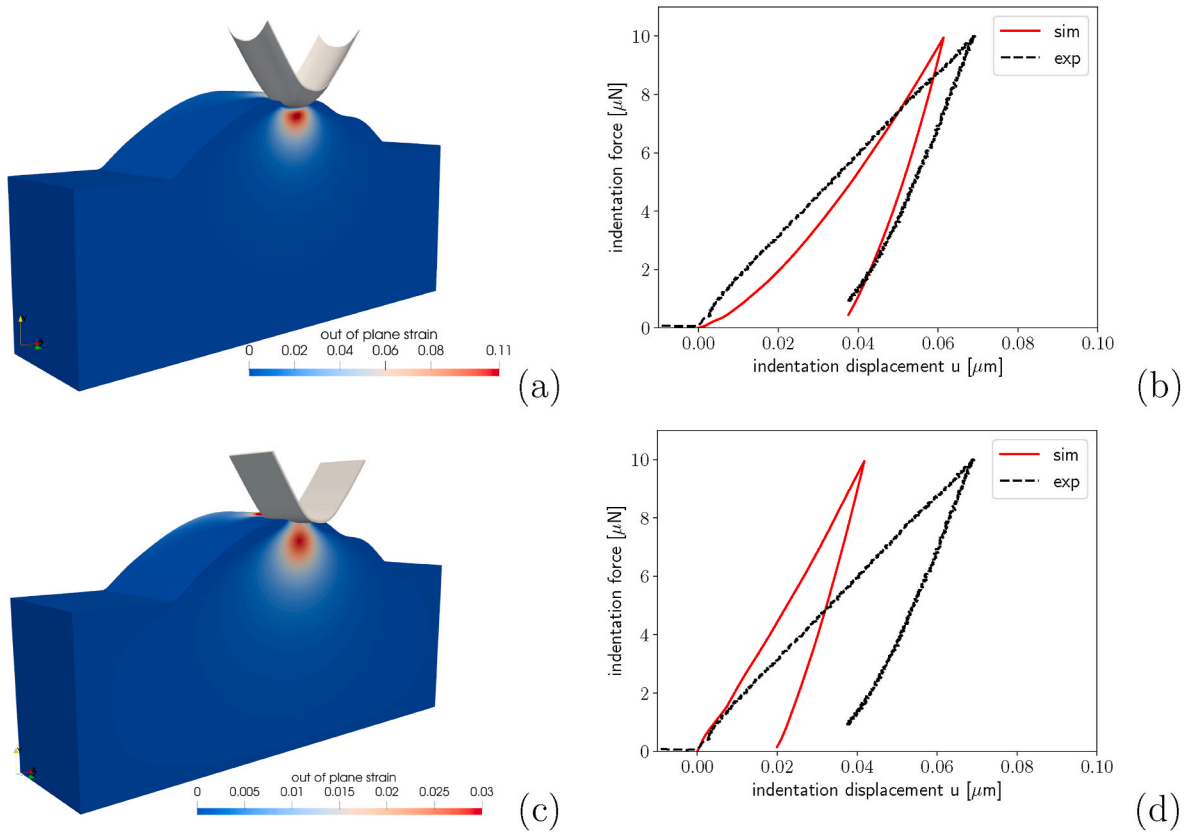

Fig. C.16. Three-dimensional simulation of the indentation problem. (a) Out-of-plane strains with the actual indenter geometry. (b) Force-displacement curve for the three-dimensional simulation pictured in (a). (c) Simplified flat indenter geometry to illustrate the reduction of out-of-plane strains due to adhesion effects. The out-of-plane strains are much smaller than in (a). (d) Force-displacement curve for the simulation in (c): A better qualitative fit is achieved in the force displacement graph; however, the 3D simulation does not match the experimental curve well due to the additional boundary influence. This influence can be observed at the backside of the indenter, where a high stress region is located. (c).

Fig. C16 (b) shows obviously a progressive loading curve in the simulation, which one would also expect from Hertz theory ($F \propto \delta^{3/2}$ (Johnson, 1985), with F being the force and δ the indentation depth). As the experiments do not indicate this curve shape – it is more linear-like – either the material or the contact geometry are the cause for the non-progressive behavior. While a material with a degressive hardening behavior could partially compensate for the curvature – after a sufficient contact area is formed – it cannot explain the initial progressive shape, as this is mainly influenced by the contact geometry. Consequently, the initial contact geometry, which is influenced by adhesion and surface roughness, is the cause of the linear-like loading curve in the experiments. Since the latter two are difficult to implement, the force-displacement curve in Fig. C16 (b) serves as an indication if the optimized parameters are of a similar order of magnitude with the three-dimensional simulation. Apart from the curves' shape, the maximum and residual indentation depth are quite close to the experimental ones. Therefore, the final plane strain parameter set can still be regarded as a good approximation for the three-dimensional problem.

In Fig. C16 (a), the out-of-plane strains are visualized, which are approximately one third of the maximum strains. Since in this simulation no out-of-plane microfibril reinforcement is considered, the strains are expected to be smaller. Furthermore, due to adhesion effects outlined in Appendix B the load is transferred more evenly over the thickness. As a result, smaller out-of-plane strains are observed as it is visible in Fig. C16 (c) with a flat indenter geometry in out-of-plane direction. The flat-indenter geometry induces unrealistic edge effects which explains the large difference to the plane strain simulation in Fig. 9 (a). However, the force-displacement curves are qualitatively similar.

Appendix D. Uniqueness of the estimated parameter sets

The fitted parameters of the numerical model (the hardening slope K, the Young's modulus μ, and the Poisson's ratio ν) are strongly coupled during optimization. In particular, we discuss the uniqueness of the optimized parameters with respect to the yield stress y_0.

To reach point 1 in the force-displacement curve while loading, both K and μ have to meet a single constraint (constraint 1), as is sketched in Fig. D17. While unloading to point 2, the material behaves purely elastic and only μ is active to meet this additional constraint (constraint 2). Hence, with these two constraints μ and K would be uniquely defined. However, the yield stress y_0 provides an additional degree of freedom, thus uniqueness would be lost. As there is no distinct change in stiffness at the yield point of the material, the parameters K and μ are of the same order. This results in an insensitivity of the optimization algorithm to the specific value of the yield stress, as displayed in Fig. D17. Many different combinations of y_0 and K give practically the same quality of fit. Hence, the optimization would either optimize K or y_0 and the other value would stay close to its starting value. As this would make a comparison of different data sets difficult, we set the yield stress a priori to a reasonable value.

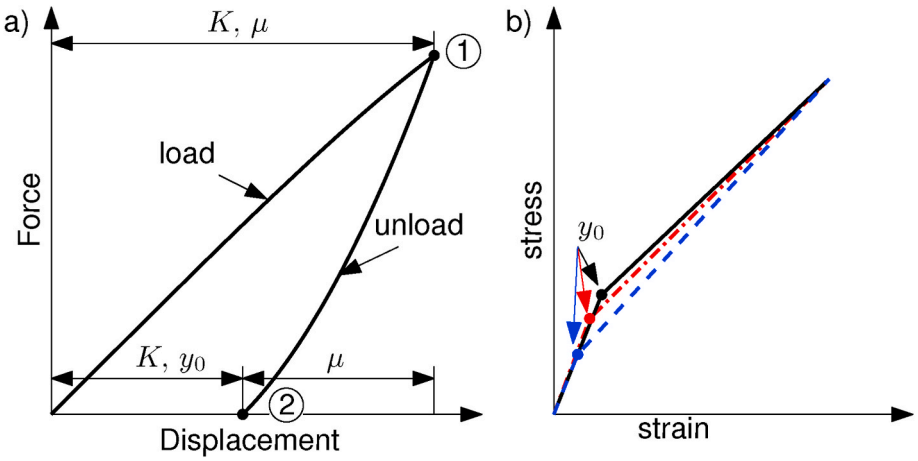

Fig. D.17. a) Influence of the parameters on the force-displacement curve. b) Small influence of the yield point if the tangent modulus during plastic deformation is close to the Young's modulus.

The determination of the Poisson's ratio ν requires an additional error to be minimized so that the problem stays determined (constraint 3, the area change). However, it should be mentioned that there is unavoidably a strong coupling between the area change and the force-displacement errors.

Appendix E. Supplementary data

Supplementary data to this article can be found online at https://doi.org/10.1016/j.mechmat.2020.103672.

References

Adusumalli, R.B., Mook, W.M., Passas, R., Schwaller, P., Michler, J., 2010a. Nanoindentation of single pulp fibre cell walls. J. Mater. Sci. 45, 2558–2563. https://doi.org/10.1007/s10853-010-4226-9.

Adusumalli, R.B., Raghavan, R., Ghisleni, R., Zimmermann, T., Michler, J., 2010b. Deformation and failure mechanism of secondary cell wall in Spruce late wood. Appl. Phys. Mater. Sci. Process 100, 447–452. https://doi.org/10.1007/s00339-010-5847-1.

Alava, M., Niskanen, K., 2006. The physics of paper. Rep. Prog. Phys. 69, 669–723. https://doi.org/10.1088/0034-4885/69/3/R03.

Alince, B., 1990. The role of porosity in polyethylenimine adsorption onto cellulosic fibers. J. Appl. Polym. Sci. 39, 355–362. https://doi.org/10.1002/app.1990.070390212.

Alince, B., 2002. Porosity of swollen pulp fibers revisited. Nord. Pulp Pap Res. J. 17, 71–73. https://doi.org/10.3183/npprj-2002-17-01-p071-073.

Barthel, E., 2008. Adhesive elastic contacts: JKR and more. J. Phys. Appl. Phys. 41, 20. https://doi.org/10.1088/0022-3727/41/16/163001.

Beex, L.A., Peerlings, R.H., 2009. An experimental and computational study of laminated paperboard creasing and folding. Int. J. Solid Struct. 46, 4192–4207. https://doi.org/10.1016/j.ijsolstr.2009.08.012.

Bergander, A., Salmén, L., 2002. Cell wall properties and their effects on the mechanical properties of fibers. J. Mater. Sci. 37, 151–156. https://doi.org/10.1023/A:1013115925679.

Bogdanovic, G., Tiberg, F., Rutland, M.W., 2001. Sliding friction between cellulose and silica surfaces. Langmuir 17, 5911–5916. https://doi.org/10.1021/la010330c.

Booker, R.E., Sell, J., 1998. The nanostructure of the cell wall of softwoods and its functions in a living tree. Holz als Roh- Werkst. 56, 1–8. https://doi.org/10.1007/s001070050255.

Borgqvist, E., Wallin, M., Ristinmaa, M., Tryding, J., 2015. An anisotropic in-plane and out-of-plane elasto-plastic continuum model for paperboard. Compos. Struct. 126, 184–195. https://doi.org/10.1016/j.compstruct.2015.02.067.

Brandberg, A., Kulachenko, A., 2017. The effect of geometry changes on the mechanical stiffness of fibre-fibre bonds. In: Batchelor, W., Söderberg, D. (Eds.), Advances in Pulp and Paper Research, Oxford 2017, Trans. Of the XVIth Fund. Res. Symp. Oxford, 2017. FRC, Manchester, pp. 683–719 doi:0.15376/frc.2017.2.683.

Chang, A.C., Liu, B.H., 2018. Modified flat-punch model for hyperelastic polymeric and biological materials in nanoindentation. Mech. Mater. 118, 17–21. https://doi.org/10.1016/j.mechmat.2017.12.010.

Chen, J., 2016. Investigation on the Mechanical Behavior of Paper and Paper Stacks in the Out-Of-Plane Direction. PhD thesis. Technische Universität Darmstadt, Darmstadt. https://tuprints.ulb.tu-darmstadt.de/id/eprint/5770.

Chen, J., Dörsam, E., Spiehl, D., Tehrani, A.H., 2018. Elastic model of paper stacks by considering the paper structure. Nord. Pulp Pap Res. J. 31, 648â€–658. https://doi.org/10.3183/npprj-2016-31-04-p648-658.

Chen, Y., Siegmund, T., 2019. Mechanics of compaction of a porous non-woven fiber solid. Mech. Mater. 137, 103101. https://doi.org/10.1016/j.mechmat.2019.103101.

Christensen, R.M., 1980. Mechanics of Composite Materials. Dover Publications, Inc., Mineola, New York.

Conners, T.E., 2001. Wood: ultrastructure. In: Buschow, K.H.J., Cahn, R.W., Flemings, M. C., Ilschner, B., Kramer, E.J., Mahajan, S., Veyssière, P. (Eds.), Encyclopedia of Materials: Science and Technology. Elsevier, Oxford, pp. 9751–9759. https://doi.org/10.1016/B0-08-043152-6/01771-X.

Cristian Neagu, R., Kristofer Gamstedt, E., Bardage, S.L., Lindström, M., 2006. Ultrastructural features affecting mechanical properties of wood fibres. Wood Mater. Sci. Eng. 1, 146–170. https://doi.org/10.1080/17480270701195374.

Czibula, C., Ganser, C., Seidlhofer, T., Teichert, C., Hirn, U., 2019. Transverse viscoelastic properties of pulp fibers investigated with an atomic force microscopy method. J. Mater. Sci. 54, 11448–11461. https://doi.org/10.1007/s10853-019-03707-1.

De Magistris, F., Salmén, L., 2008. Finite Element modelling of wood cell deformation transverse to the fibre axis. Nord. Pulp Pap Res. J. 23, 240–246. https://doi.org/10.3183/NPPRJ-2008-23-02-p240-246.

Deshpande, V.S., Fleck, N.A., 2000. Isotropic constitutive models for metallic foams. J. Mech. Phys. Solid. 48, 1253–1283. https://doi.org/10.1016/S0022-5096(99)00082-4.

Dhondt, G., 2004. The Finite Element Method for Three-Dimensional Thermomechanical Applications. John Wiley & Sons, Ltd, Chichester, UK. https://doi.org/10.1002/0470021217.

Dumbleton, D.F., 1972. Longitudinal compression of individual pulp fibres. TAPPI (Tech. Assoc. Pulp Pap. Ind.) 55, 127–135.

Dunford, J.A., Wild, P.M., 2002. Cyclic transverse compression of single wood-pulp fibres. J. Pulp Pap. Sci. 28, 136–141.

Eder, M., Arnould, O., Dunlop, J.W., Hornatowska, J., Salmén, L., 2013. Experimental micromechanical characterisation of wood cell walls. Wood Sci. Technol. 47, 163–182. https://doi.org/10.1007/s00226-012-0515-6.

EDF, 2020. Finite Element Code_aster, Analysis of Structures and Thermomechanics for Studies and Research.

Fahlén, J., Salmén, L., 2005. Pore and matrix distribution in the fiber wall revealed by atomic force microscopy and image analysis. Biomacromolecules 6, 433–438. https://doi.org/10.1021/bm040068x.

Feng, G., Ngan, A., 2002. Effects of creep and thermal drift on modulus measurement using depth-sensing indentation. J. Mater. Res. 17, 660–668.

Fischer-Cripps, A., 2000. A review of analysis methods for sub-micron indentation testing. Vacuum 58, 569–585. https://doi.org/10.1016/S0042-207X(00)00377-8.

Fritzen, F., Forest, S., Kondo, D., Böhlke, T., 2013. Computational homogenization of porous materials of Green type. Comput. Mech. 52, 121–134. https://doi.org/10.1007/s00466-012-0801-z.

Ganser, C., Hirn, U., Rohm, S., Schennach, R., Teichert, C., 2014. AFM nanoindentation of pulp fibers and thin cellulose films at varying relative humidity. Holzforschung 68, 53–60. https://doi.org/10.1515/hf-2013-0014.

Ganser, C., Teichert, C., 2017. AFM-based nanoindentation of cellulosic fibers. In: Tiwari, A., Natarajan, S. (Eds.), Applied Nanoindentation in Advanced Materials. John Wiley & Sons, Chichester, UK and Hoboken, NJ, pp. 247–267. https://doi.org/10.1002/9781119084501.

Geuzaine, C., Remacle, J.F., 2009. Gmsh: a 3-D finite element mesh generator with built-in pre- and post-processing facilities. Int. J. Numer. Methods Eng. 79, 1309–1331. https://doi.org/10.1002/nme.2579.

Gibson, L.J., 2012. The hierarchical structure and mechanics of plant materials. J. R. Soc. Interface 9, 2749–2766. https://doi.org/10.1098/rsif.2012.0341.

Gill, P.E., Murray, W., Wright, M.H., 1981. Practical Optimization. Academic Press, London.
Gindl, W., Gupta, H.S., Schöberl, T., Lichtenegger, H.C., Fratzl, P., 2004. Mechanical properties of spruce wood cell walls by nanoindentation. Appl. Phys. Mater. Sci. Process 79, 2069–2073. https://doi.org/10.1007/s00339-004-2864-y.
Gindl, W., Schöberl, T., 2004. The significance of the elastic modulus of wood cell walls obtained from nanoindentation measurements. Compos. Appl. Sci. Manuf. 35, 1345–1349. https://doi.org/10.1016/j.compositesa.2004.04.002.
Godinho, P.M.J., Jajcinovic, M., Wagner, L., Vass, V., Fischer, W.J., Bader, T.K., Hirn, U., Bauer, W., Eberhardsteiner, J., Hellmich, C., 2019. A continuum micromechanics approach to the elasticity and strength of planar fiber networks: theory and application to paper sheets. Eur. J. Mech. Solid. 75, 516–531. https://doi.org/10.1016/j.euromechsol.2018.10.005.
Gray, J.S., Hwang, J.T., Martins, J.R.R.A., Moore, K.T., Naylor, B.A., 2019. OpenMDAO: an open-source framework for multidisciplinary design, analysis, and optimization. Struct. Multidiscip. Optim. 59, 1075–1104. https://doi.org/10.1007/s00158-019-02211-z.
Green, R.J., 1972. A plasticity theory for porous solids. Int. J. mech. Sci. Pergamon Press 14, 215–224.
Hardacker, K., 1969. Cross-sectional area measurement of individual wood pulp fibres by lateral compaction. TAPPI (Tech. Assoc. Pulp Pap. Ind.) 52, 1742–1746.
Hartler, N., Nyrén, J., 1970. Transverse Compressibility of pulp fibers. 2. Influence of cooking method, yield, beating, and drying. TAPPI (Tech. Assoc. Pulp Pap. Ind.) 53, 820–823.
Helfer, T., Michel, B., Proix, J.M., Salvo, M., Sercombe, J., Casella, M., 2015. Introducing the open-source mfront code generator: application to mechanical behaviours and material knowledge management within the PLEIADES fuel element modelling platform. Comput. Math. Appl. 70, 994–1023. https://doi.org/10.1016/j.camwa.2015.06.027.
Hossain, M.S., Bergström, P., Uesaka, T., 2019. Uniaxial compression of three-dimensional entangled fibre networks: impacts of contact interactions. Model. Simulat. Mater. Sci. Eng. 27 https://doi.org/10.1088/1361-651X/aaf1ed.
Hutter, J.L., Bechhoefer, J., 1993. Calibration of atomic-force microscope tips. Rev. Sci. Instrum. 64, 1868–1873. https://doi.org/10.1063/1.1143970.
Jäger, A., Bader, T., Hofstetter, K., Eberhardsteiner, J., 2011. The relation between indentation modulus, microfibril angle, and elastic properties of wood cell walls. Compos. Appl. Sci. Manuf. 42, 677–685. https://doi.org/10.1016/j.compositesa.2011.02.007.
Johnson, K.L., 1985. Contact Mechanics, 9 ed. Cambridge university press, Cambridge.
Kendall, K., 2001. Molecular Adhesion and its Applications. Kluwer Academic/Plenum Publishers, New York.
Kim, S., Shin, H., Rhim, S., Rhee, K.Y., 2019. Calibration of hyperelastic and hyperfoam constitutive models for an indentation event of rigid polyurethane foam. Compos. B Eng. 163, 297–302. https://doi.org/10.1016/j.compositesb.2018.11.045.
Kolymbas, D., 1991. An outline of hypoplasticity. Arch. Appl. Mech. 61, 143–151. https://doi.org/10.1007/BF00788048.
Kolymbas, D., Medicus, G., 2016. Genealogy of hypoplasticity and barodesy. Int. J. Numer. Anal. Methods GeoMech. 40, 2532–2550. https://doi.org/10.1002/nag.2546.
Kuhn, M.R., 1999. Structured deformation in granular materials. Mech. Mater. 31, 407–429. https://doi.org/10.1016/S0167-6636(99)00010-1.
Li, Y., Stapleton, S.E., Reese, S., Simon, J.W., 2018. Anisotropic elastic-plastic deformation of paper: out-of-plane model. Int. J. Solid Struct. 130–131, 172–182. https://doi.org/10.1016/j.ijsolstr.2017.10.003.
Lorbach, C., Hirn, U., Kritzinger, J., Bauer, W., 2012. Automated 3D measurement of fiber cross section morphology in handsheets. Nord. Pulp Pap Res. J. 27, 264–269. https://doi.org/10.3183/NPPRJ-2012-27-02-p264-269.
Lovikka, V.A., Khanjani, P., Väisänen, S., Vuorinen, T., Maloney, T.C., 2016. Porosity of wood pulp fibers in the wet and highly open dry state. Microporous Mesoporous Mater. 234, 326–335. https://doi.org/10.1016/j.micromeso.2016.07.032.
Maloney, T.C., Paulapuro, H., 1999. The formation of pores in the cell wall. J. Pulp Pap. Sci. 25, 430–436.
Mark, R.E., 1983. Handbook of Physical and Mechanical Testing of Paper and Paperboard, vol. 1. Dekker, New York.
Medicus, G., Schneider-Muntau, B., 2019. Simulations of fine-meshed biaxial tests with Barodesy. Geosciences 9, 1–17. https://doi.org/10.3390/geosciences9010020.
Medicus, G., Schneider-Muntau, B., Kolymbas, D., 2019. Second-order work in barodesy. Acta Geotechnica 14, 1483–1493. https://doi.org/10.1007/s11440-018-0749-z.
Miehe, C., Apel, N., Lambrecht, M., 2002. Anisotropic additive plasticity in the logarithmic strain space: modular kinematic formulation and implementation based on incremental minimization principles for standard materials. Comput. Methods Appl. Mech. Eng. 191, 5383–5425. https://doi.org/10.1016/S0045-7825(02)00438-3.
Morin, C., Avril, S., Hellmich, C., 2018. Non-affine fiber kinematics in arterial mechanics: a continuum micromechanical investigation. ZAMM Zeitschrift für Angewandte Mathematik und Mechanik 98, 2101–2121. https://doi.org/10.1002/zamm.201700360.
Nečas, D., Klapetek, P., 2012. Gwyddion: an open-source software for SPM data analysis. Cent. Eur. J. Phys. 10, 181–188. https://doi.org/10.2478/s11534-011-0096-2.
Netzker, C., Dal, H., Kaliske, M., 2010. An endochronic plasticity formulation for filled rubber. Int. J. Solid Struct. 47, 2371–2379. https://doi.org/10.1016/j.ijsolstr.2010.04.026.
Nilsson, B., Wagberg, L., Gray, D., 2001. Conformability of wet pulp fibres at small length scales. In: Proc. 12th Fundamental Research Symposium, Oxford, pp. 211–224.
Niskanen, K., 1998. Papermaking Science and Technology: Paper Physics, 16 ed. Fapet Oy.
Oliver, W.C., Pharr, G., 1992. An improved technique for determining hardness and elastic modulus using load and displacement sensing indentation experiments. J. Mater. Res. 7, 1564–1583. https://doi.org/10.1557/JMR.1992.1564.
Park, S., Venditti, R.A., Jameel, H., Pawlak, J.J., 2006. Changes in pore size distribution during the drying of cellulose fibers as measured by differential scanning calorimetry. Carbohydr. Polym. 66, 97–103. https://doi.org/10.1016/j.carbpol.2006.02.026.
Patterson, B.M., Cordes, N.L., Henderson, K., Williams, J.J., Stannard, T., Singh, S.S., Ovejero, A.R., Xiao, X., Robinson, M., Chawla, N., 2015. In situ X-ray synchrotron tomographic imaging during the compression of hyper-elastic polymeric materials. J. Mater. Sci. 51, 171–187. https://doi.org/10.1007/s10853-015-9355-8.
Persson, B.N., Ganser, C., Schmied, F., Teichert, C., Schennach, R., Gilli, E., Hirn, U., 2013. Adhesion of cellulose fibers in paper. J. Phys. Condens. Matter 25. https://doi.org/10.1088/0953-8984/25/4/045002.
Peters, J.F., Muthuswamy, M., Wibowo, J., Tordesillas, A., 2005. Characterization of force chains in granular material. Phys. Rev. E - Stat. Nonlinear Soft Matter Phys. 72 https://doi.org/10.1103/PhysRevE.72.041307.
Rajagopal, K., Srinivasa, A., 2009. On a class of non-dissipative materials that are not hyperelastic. Proc. Math. Phys. Eng. Sci. 465, 493–500. https://doi.org/10.1098/rspa.2008.0319.
Rajagopal, K.R., 2007. The elasticity of elasticity. Zeitschrift fur Angewandte Mathematik und Physik 58, 309–317. https://doi.org/10.1007/s00033-006-6084-5.
Rajagopal, K.R., Srinivasa, A.R., 2011. A Gibbs-potential-based formulation for obtaining the response functions for a class of viscoelastic materials. Proc. Math. Phys. Eng. Sci. 467, 39–58. https://doi.org/10.1098/rspa.2010.0136.
Rinde, J.A., 1970. Poisson's ratio for rigid plastic foams. J. Appl. Polym. Sci. 14, 1913–1926. https://doi.org/10.1002/app.1970.070140801.
Salmén, L., 2018. Wood cell wall structure and organisation in relation to mechanics. In: Geitmann, A., Gril, J. (Eds.), Plant Biomechanics. Springer International Publishing, pp. 3–19. https://doi.org/10.1007/978-3-319-79099-2_1.
Sanborn, B., Song, B., 2019. Poisson's ratio of a hyperelastic foam under quasi-static and dynamic loading. Int. J. Impact Eng. 123, 48–55. https://doi.org/10.1016/j.ijimpeng.2018.06.001.
Schmied, F.J., Teichert, C., Kappel, L., Hirn, U., Schennach, R., 2012. Joint strength measurements of individual fiber-fiber bonds: an atomic force microscopy based method. Rev. Sci. Instrum. 83 https://doi.org/10.1063/1.4731010, 073902–1.
Sedighi-Gilani, M., Navi, P., 2007. Experimental observations and micromechanical modeling of successive-damaging phenomenon in wood cells' tensile behavior. Wood Sci. Technol. 41, 69–85. https://doi.org/10.1007/s00226-006-0094-5.
Seidlhofer, T., Czibula, C., Teichert, C., Payerl, C., Hirn, U., Ulz, M.H., 2019. A minimal continuum representation of a transverse isotropic viscoelastic pulp fibre based on micromechanical measurements. Mech. Mater. 135, 149–161. https://doi.org/10.1016/j.mechmat.2019.04.012.
Shiari, B., Wild, P.M., 2004. Finite element analysis of individual wood-pulp fibers subjected to transverse compression. Wood Fiber Sci. 36, 135–142.
Simulia, D., 2009. ABAQUS/Standard User's Manual. DS Simulia, Version 6.9.
Stone, J.E., Scallan, A.M., 1965. Effect of component removal upon the porous structure of the cell wall of wood. J. Polym. Sci., Polym. Chem. Ed. 11, 13–25.
Storåkers, B., 1986. On material representation and constitutive branching in finite compressible elasticity. J. Mech. Phys. Solid. 34, 125–145. https://doi.org/10.1016/0022-5096(86)90033-5.
Suchocki, C., Skoczylas, P., 2016. Finite strain formulation of elasto-plasticity without yield surface: theory, parameter identification and applications. J. Theor. Appl. Mech. 54, 731–742. https://doi.org/10.15632/jtam-pl.54.3.731.
Tang, B., Ngan, A.H.W., 2003. Accurate measurement of tipâ€"sample contact size during nanoindentation of viscoelastic materials. J. Mater. Res. 18, 1141–1148. https://doi.org/10.1557/JMR.2003.0156.
Truesdell, C., Noll, W., Antman, S.S., 2004. The Non-linear Field Theories of Mechanics, 3 ed. Springer, Berlin, Heidelberg, New York.
Villarrubia, J., 1994. Morphological estimation of tip geometry for scanned probe microscopy. Surf. Sci. 321, 287–300. https://doi.org/10.1016/0039-6028(94)90194-5.
Virtanen, P., Gommers, R., Oliphant, T.E., Haberland, M., Reddy, T., Cournapeau, D., Burovski, E., Peterson, P., Weckesser, W., Bright, J., van der Walt, S.J., Brett, M., Wilson, J., Jarrod Millman, K., Mayorov, N., Nelson, A.R.J., Jones, E., Kern, R., Larson, E., Carey, C., Polat, İ., Feng, Y., Moore, E.W., Vand erPlas, J., Laxalde, D., Perktold, J., Cimrman, R., Henriksen, I., Quintero, E.A., Harris, C.R., Archibald, A. M., Ribeiro, A.H., Pedregosa, F., van Mulbregt, P., Contributors, S., et al., 2020. Scipy 1.0: fundamental algorithms for scientific computing in python. Nat. Methods 17, 261–272. https://doi.org/10.1038/s41592-019-0686-2.
Wallmeier, M., Linvill, E., Hauptmann, M., Majschak, J.P., Östlund, S., 2015. Explicit FEM analysis of the deep drawing of paperboard. Mech. Mater. 89, 202–215. https://doi.org/10.1016/j.mechmat.2015.06.014.
Wild, P., Omholt, I., Steinke, D., Schuetze, A., 2005. Experimental characterization of the behaviour of wet single wood-pulp fibres under transverse compression. J. Pulp Pap. Sci. 31, 116–120.
Wimmer, R., Lucas, B.H., Tsui, T.Y., Oliver, W.C., 1997. Longitudinal hardness and Young's modulus of spruce tracheid secondary walls using nanoindentation technique. Wood Sci. Technol. 31, 131–141. https://doi.org/10.1007/BF00705928.
Yan, D., Li, K., 2013. Conformability of wood fiber surface determined by AFM indentation. J. Mater. Sci. 48, 322–331. https://doi.org/10.1007/s10853-012-6749-8.
Zerbe, P., Schneider, B., Moosbrugger, E., Kaliske, M., 2017. A viscoelastic-viscoplastic-damage model for creep and recovery of a semicrystalline thermoplastic. Int. J. Solid Struct. 110–111, 340–350. https://doi.org/10.1016/j.ijsolstr.2016.10.029.